Ambient Noise Analysis in the Eastern Sea of Marmara Region in Northwest Turkey: Lateral Variations of the Crustal Velocity Field

by Diğdem Acarel, Fatih Bulut, and Marco Bohnhoff[*]

Abstract   We analyze the ambient seismic-noise field in order to investigate the crustal structure at the North Anatolian fault zone (NAFZ) in northwest Turkey. We focus on the eastern Sea of Marmara section, where the NAFZ is in the final phase of the seismic cycle prior to an expected major ($M > 7$) earthquake. We apply cross-correlation analysis of the seismic ambient noise to determine the spectral dependence of the seismic velocity in order to image the crustal structure at seismogenic depth. Time-domain cross correlations are calculated for available station pairs in the target area. Interstation distances span 0.3–90 km. Here, the vertical component is analyzed in order to recover fundamental-mode Rayleigh waves in the 0.05–1.1 Hz frequency range. Group velocity dispersion curves are obtained for selected correlation paths in particular to address the azimuthal dependence of the velocity field. In the frequency band of interest, average group velocities range between ~1.8 and 3.5 km/s. Dispersion curves corresponding to the north–south-trending paths crossing the main NAFZ fault branch below the eastern Sea of Marmara show low group velocities between ~1.5 and 1.8 km/s, which is well explained by the 3–4 km-deep Çınarcık basin, located between the two major fault branches, the Princes Islands and Armutlu fault segments. In contrast, ray paths restricted to within the mainland of Istanbul and the Armutlu peninsulas (primarily trending east–west) show higher group velocities up to 3.2 km/s. By averaging the dispersion curves, we determine an optimized 1D S-wave velocity model for the eastern Sea of Marmara region, allowing for a significant improvement in hypocenter determination for local seismicity.

Introduction and Tectonic Setting

The Earth's surface vibrates continuously over a wide frequency range, providing continuous sampling of the Earth's interior at different spatial scales without the need of earthquakes or man-made sources. These vibrations, or ambient noise, can be induced by natural or anthropogenic sources (Asten, 1978; Asten and Henstridge, 1984; Bonnefoy-Claudet *et al.*, 2004). The long period range of the noise spectrum is covered by the microseisms representing the response of natural sources (e.g., atmospheric disturbances or interaction of ocean gravity waves with the coastlines). The higher frequency range is predominantly characterized by microtremors resulting from anthropogenic sources or local meteorological events. The transition range between the frequency content of microseisms and microtremors is not sharp and might vary regionally (Bonnefoy-Claudet *et al.*, 2004). Amplitude variations of microseisms are mostly controlled by oceanic activity or large-scale meteorological events, whereas the amplitude of microtremors might correlate with variable human activities during working hours/days.

Cross correlations of the ambient seismic noise field recorded at different seismic stations currently are applied at local and regional scales to investigate the velocity field from near-surface down to crustal and upper-mantle depths (e.g., Shapiro *et al.*, 2005; Lin *et al.*, 2008; Renalier *et al.*, 2010). The cross correlations of ambient noise recordings between station pairs give an approximate Green's function for the surface-wave propagation within the relevant medium (Shapiro and Campillo, 2004). Furthermore, Shapiro *et al.* (2005) showed that in the same frequency band, the surface-wave response at one station to an earthquake that occurred in the vicinity of the other station is almost identical to the Green's function emerging from the cross correlation between these two stations. This knowledge is used to obtain the frequency dependence of seismic velocities (dispersion) between the station pairs and then to derive the structural

*Also at Free University Berlin, Institute of Geological Sciences, Berlin, Germany.
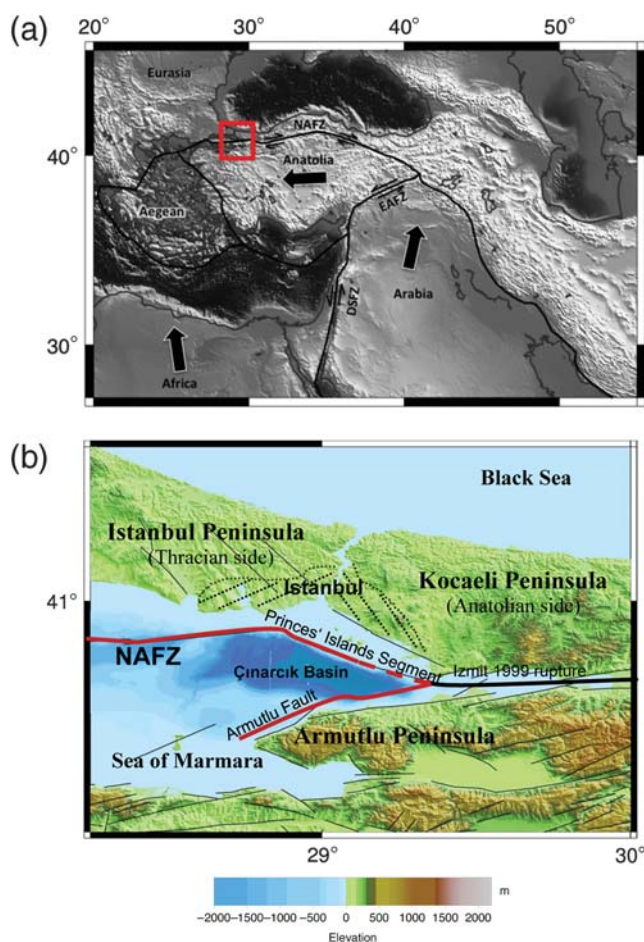
Figure 1. (a) Location map of the larger eastern Mediterranean–Anatolian–Arabian region. Major plate boundaries (after Bird, 2003) are indicated by black lines, and Global Positioning System-derived plate motions (with respect to fixed Eurasia) are shown by black arrows. The target area is indicated by the red square and enlarged in (b). (b) Eastern Sea of Marmara region in northwestern Turkey, with major tectonic elements and the main branches of the North Anatolian fault zone (NAFZ; red lines). The dotted lines show the extent of the city of Istanbul. The bold black line shows the western part of the 1999 Izmit earthquake rupture, and black lines are secondary faults throughout the region (Gülen et al., 2002). (Topography, SRTM30 grid; bathymetry, Armijo et al., 2002.)

variations of the medium at various scales. Consequently, the ambient noise field provides a large database for structural investigations, especially in areas with insufficient numbers of earthquakes. Green's functions derived from cross correlations have been used to determine, for example, crustal structures along and across active plate boundaries (Shapiro et al., 2005; Bensen et al., 2008; Lin et al., 2008); to simulate ground motion in central Mexico (Chavez-Garcia and Quintanar, 2010); and to obtain 3D shear-wave velocity models of the Patagonian crust above the subducting Chile ridge (Gallego et al., 2010) and in the Gyeongsang basin, one of the major structural components of the Korean Peninsula (Cho et al., 2007).

In this study, we focus on ambient noise recordings in the eastern Sea of Marmara region, northwest Turkey. There,

the North Anatolian fault zone (NAFZ) is currently in the final stage of the seismic cycle, and the probability of a major (M > 7) earthquake is 35%–70% within the next 30 years (Parsons, 2004). Our main focus is to image the velocity field along and across the Princes Islands segment of the NAFZ, bounding the Çınarcık basin offshore of the large population center of Istanbul, with its > 13 million inhabitants (Fig. 1). As the major NAFZ fault branch below the Sea of Marmara, this segment has not been activated since 1766 and is located at the transition to the 1999 Izmit rupture (e.g., Bulut et al., 2009, 2011; Bohnhoff et al., 2013). The Çınarcık basin is a wedge-shaped half-graben structure representing a pull-apart basin in the eastern part of the Sea of Marmara. It covers a 50×20 km wide area at a maximum seafloor depth of ~1250 m. The sediment fill reaches up to ~3.5 km (Karabulut et al., 2003; Carton et al., 2007).

We analyze the ambient seismic noise field using the continuous seismic recordings from selected seismic stations deployed throughout the target area. The lateral variation of seismic velocity within the crustal blocks framing the NAFZ and across the Princes Islands segment and the Çınarcık basin is studied and related with the regional microseismicity in order to better understand the relation between the structural asymmetry and fracture networks and their role in the near vicinity of Istanbul.

Database and Evaluation

We use a total of 18 stations with interstation distances varying between 300 m and 90 km throughout the eastern Sea of Marmara area surrounding the Princes Islands segment (Fig. 2a). Although closely spaced stations are located on the Princes Islands offshore of Istanbul as part of the permanent Princes Islands High Resolution Seismic (PIRES) network, installed in 2006 (Bulut et al., 2009, 2011; Bohnhoff et al., 2013), we also include individual regional stations from the nationwide seismic networks operated by the Kandilli Observatory and Earthquake Research Institute in Istanbul (KOERI) and the Turkish Disaster and Emergency Presidency in Ankara (AFAD). Furthermore, we also include selected stations of the regional permanent network covering the greater Armutlu peninsula area (ARNET; Tunç et al., 2011). Except for the PIRES stations all selected stations are located on the mainlands surrounding the eastern Sea of Marmara (Fig. 2a).

In a first step, we perform time-domain correlations on the vertical components and thus focus on the Rayleigh-wave velocity. Prior to the preprocessing, all waveform recordings are uniformly resampled to 20 Hz. We follow the data preprocessing steps as described in Bensen et al. (2007): First, the mean, trend, and instrument response are removed. In a second step, one-bit normalization is applied in order to reduce the potential contamination of the continuous data by earthquake signals and instrumental irregularities. Finally, we apply spectral whitening to balance the frequency spectrum. We calculate correlations without band-pass
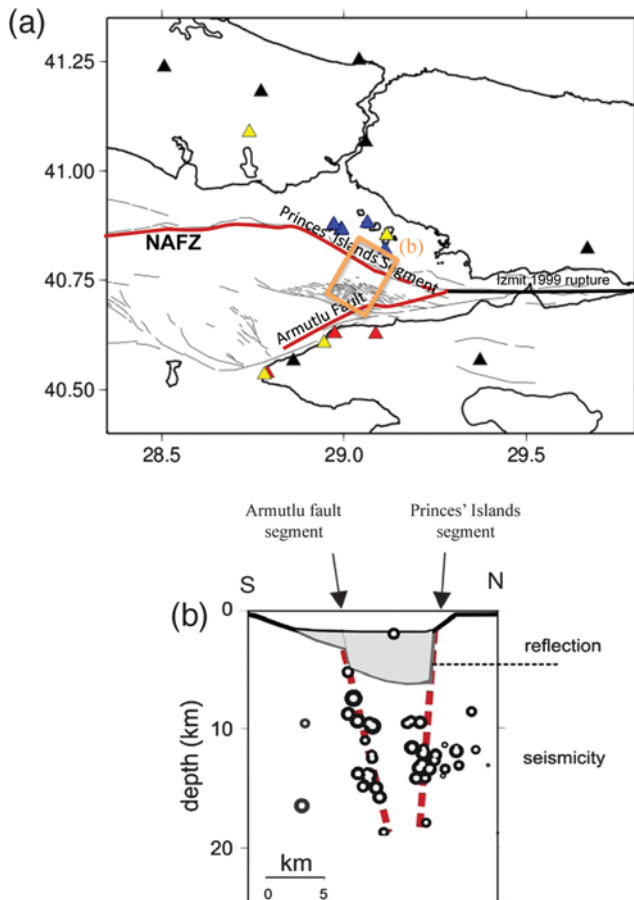
Figure 2. (a) Seismic stations used in this study, framing the Princes Islands segment of the NAFZ below the eastern Sea of Marmara. Colors indicate different networks (blue, PIRES; black, Kandilli Observatory and Earthquake Research Institute in Istanbul [KOERI], red, Armutlu peninsula area [ARNET]; yellow, Turkish Disaster and Emergency Presidency in Ankara [AFAD], respectively. See text for details.). Orange rectangle illustrates the position of the depth section shown in (b). (b) Depth section in which gray shading denotes the sediments of the Çınarcık basin (after Carton et al., 2007) and circles are hypocenters of local seismicity, allowing imaging of the down-dip extension of the two major NAFZ branches (after Bulut et al., 2009).

filtering the data so as not to lose any information contained in the waveform recordings.

Time-Domain Cross Correlations and Dispersion

A database of stacked cross correlations of each station pair is generated from one-year long continuous seismic recordings. Different lengths for correlation time windows of 1, 2, 5, 10, 30, and 60 minutes are tested, and no significant improvement is observed in the signal-to-noise ratio in the case of longer time windows. The shorter correlation time windows provide better stability, as well as the symmetry of Green's functions. On the other hand, the correlation window lengths should be long enough to simultaneously have the same signal package at different stations where the interstation distances reach up to 90 km. The correlations presented

in this study are computed by stacking nonoverlapping 5-minute-long time windows moving along a 1-year-long data stream, obtained from 18 stations and thus corresponding to ~150 correlation pairs. Time-domain correlations resulting in a low signal-to-noise ratio (below 2 dB) are discarded from further analysis. In Figure 3, the correlations stacked over time periods of 2, 5, 15, and 60 days (stacking time windows) are shown to demonstrate the improvement in the obtained Green's function by stacking for longer time windows. We find a stack of 60-day correlations is generally sufficient to obtain reliable Green's functions. However, to ensure the stabilization of the Green's functions and to achieve the best possible resolution, especially for large interstation spacing (~90 km), we focus on a longer stacking time period (~365 days).

To study the velocity field within the different crustal units throughout the area of investigation, we subdivide the station pairs into three subsets with ray paths covering individual tectonic units: the mainland and shelf north of the Princes Islands segment (northern block, including the Istanbul and Kocaeli peninsulas), the Çınarcık basin directly south of the Princes Islands segment, and the southern mainland and shelf south of the eastern Sea of Marmara (southern block, including the Armutlu peninsula; Figs. 1 and 2a). These tectonic units are analyzed separately and with respect to each other. In Figure 4, the left panel shows the ray paths of the respective station pairs and the right panel shows the corresponding cross correlations. All the ray paths considered for a particular area and corresponding cross correlations are plotted in black for the northern block (Fig. 4c,d), the Çınarcık basin (Fig. 4e,f), and southern block (Fig. 4g,h), respectively. There is a slight but systematic difference in the arrival times of the Green's function envelopes of correlations calculated within the northern (Fig. 4d) and southern blocks (Fig. 4h), compared with those for the Çınarcık basin (Fig. 4f). Based on the available station pairs, the ray coverage is better within the northern block. Moreover, the correlations obtained for the northern block are more robust (have clearer Green's functions) than those for the southern block. The correlations related to the ray paths crossing the fault zone and the Çınarcık basin suggest slower group velocities than the correlations obtained from the northern and southern block at comparable interstation distance (Fig. 4f).

In order to obtain the group velocities related to each ray path, we apply a narrow Gaussian filter with a bandwidth of 0.07 for each cross-correlation envelope to discretely extract the frequency-dependent velocity within the frequency band of interest (0.05–1.1 Hz). We use a standard derivative approach to select the maxima of the envelopes of the Gaussian-filtered cross-correlation functions in order to determine the corresponding arrival time. In Figure 5a, the shift in the arrival times of each cross-correlation envelope is shown for different frequencies. Using this information, the group velocities for the frequency band of interest (group velocity dispersion curve) can be obtained as shown in Figure 5b. The dispersion curve shows the variation of group velocity with frequency. The lower frequencies sample
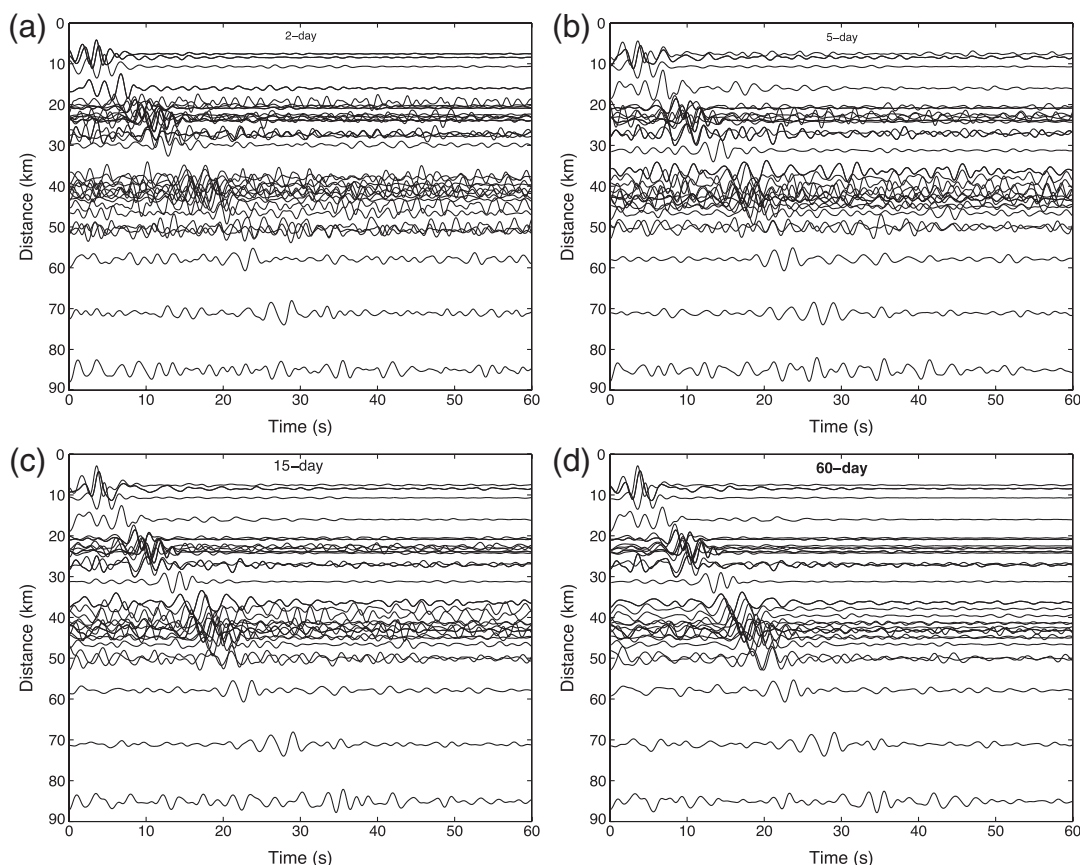
Figure 3. Stack of time-domain correlations obtained from (a) 2-day, (b) 5-day, (c) 15-day, and (d) 60-day long waveform data, respectively. The diagrams reflect an improving quality of the correlations for longer time intervals.

relatively deeper layers and therefore generally exhibit higher velocities, whereas the higher frequencies sample relatively shallower layers displaying lower group velocities.

To study potential azimuthal variations of the velocity field within and between the northern (Fig. 4c,d) and southern blocks (Fig. 4g,h), we studied the correlations of respective station pairs separately. All the ray paths and corresponding time-domain correlations are shown in Figure 4a and b. However, due to the comparatively lower data quality in the south and limited capability of short-period stations to resolve large distances, our results are restricted to the rather small number of correlation paths between broadband stations that are crossing the Çınarcık basin. The correlations obtained on the northern block yield to more reliable and faster converging Green's functions. Later arrival times in the correlations are observed along the ray paths between the northern and southern stations, which are crossing the fault zone (Fig. 4e,f). The fact that velocities are slower here is well explained by the ~3.5 km thick sediments of the Çınarcık basin (Karabulut *et al.*, 2003; Carton *et al.*, 2007), through which the waves are passing (Fig. 2b).

Dispersion curves reflecting the best obtained results and corresponding ray paths are shown in Figure 6. The results are split into three subsets based on interstation distance and the region covered by the propagation paths. We elaborate on the

results with respect to four main geologic units: namely the Istanbul Peninsula (western part of the northern block), the Kocaeli Peninsula (eastern part of the northern block), the Çınarcık basin, and the Armutlu Peninsula (southern block).

The first subset contains four ray paths over the propagation distance of 50 km (Fig. 6a,b). They also allow investigation of the surface-wave velocity for the low-frequency range (down to 0.05 Hz) due to the relatively long interstation distance (Fig. 6b). Two out of the four rays travel from the Istanbul Peninsula toward the Kocaeli Peninsula along a similar path, resulting in similar dispersion curves that reflect a group velocity between 2.5 and 3.2 km/s for the 0.05–0.5 Hz frequency range (light blue line). The other two ray paths travel from the Istanbul peninsula to the Armutlu peninsula across the eastern Sea of Marmara, with one crossing the Çınarcık basin (green line) and one passing east of the Çınarcık basin (dark blue line). The corresponding dispersion curves show the Çınarcık basin dramatically lowers the seismic velocity for Rayleigh waves down to 1.8 km/s for frequencies above 0.2 Hz (green line), whereas the path passing the fault zone east of the Çınarcık basin reflects higher values ranging between 2.0 and 3.5 km/s for the same frequency range (blue line).

The second subset contains relatively shorter ray paths sampling the subsurface of the Istanbul Peninsula and the
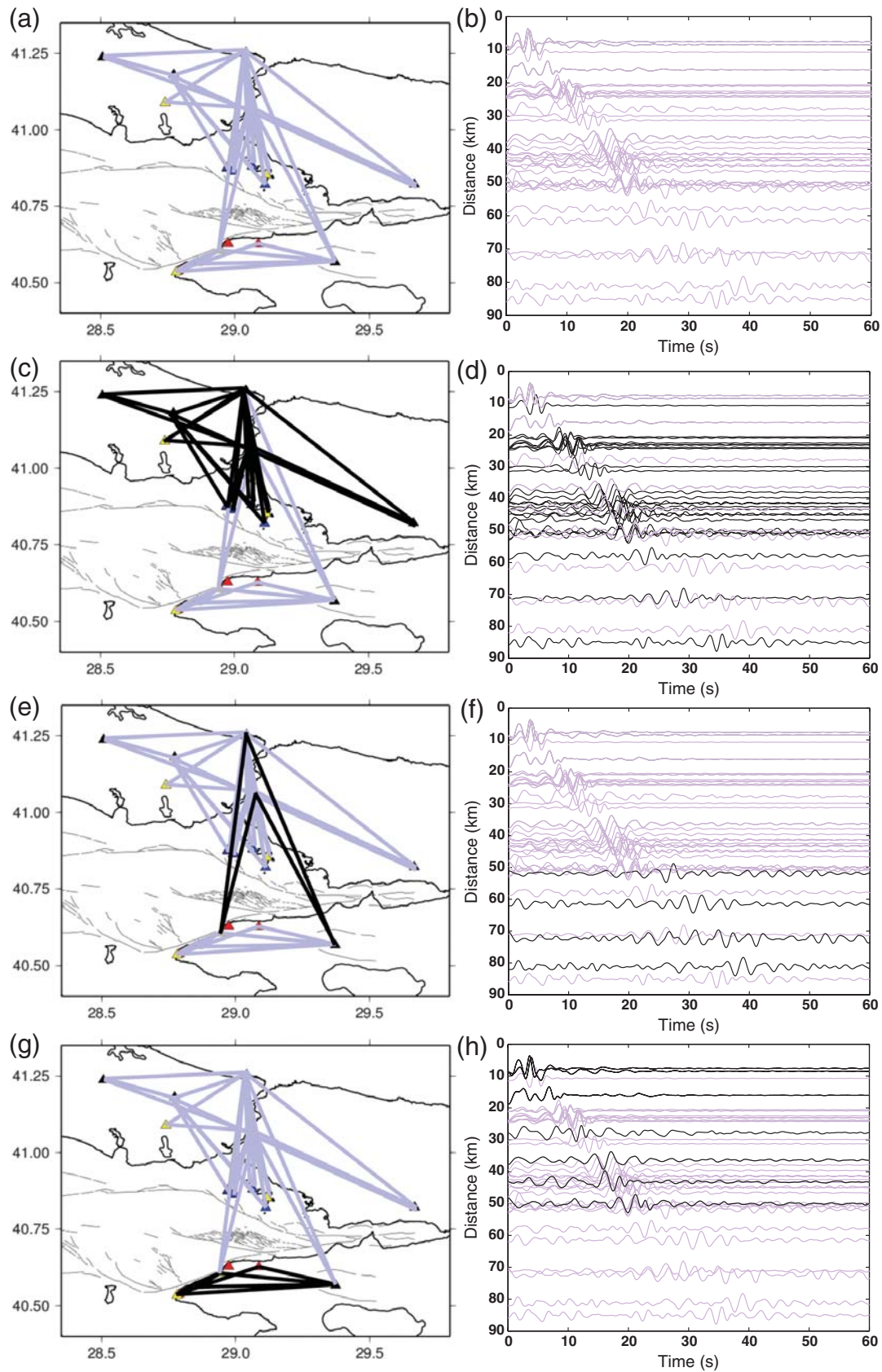
Figure 4.   (a) and (b) are stations pairs (left panel) and resulting cross correlations (right panel) for all station pairs analyzed in this study. Bold black lines highlight (c, d) station pairs with ray paths covering the Istanbul and Kocaeli peninsulas (northern block); (e, f) the eastern Sea of Marmara, including the Çınarcık basin; and (g, h) the Armutlu peninsula (southern block).
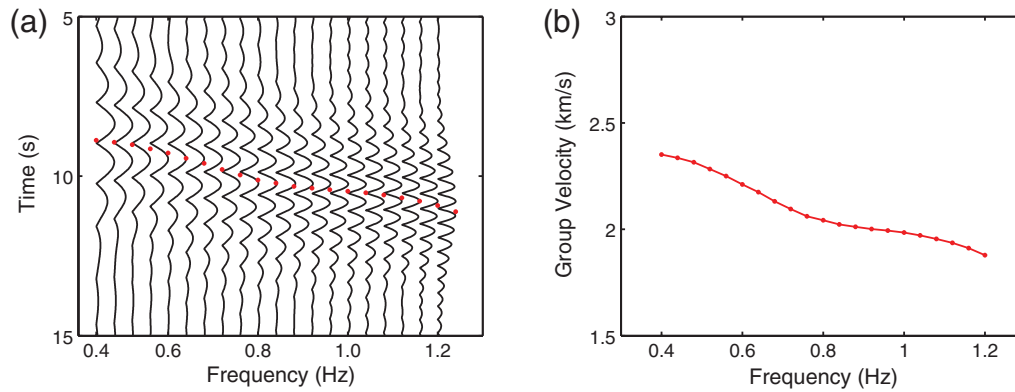
Figure 5.   (a) Absolute value of subharmonics obtained by applying a Gaussian filter to the stacked cross correlation for a station pair located in the northern block within the 0.2–1.2 Hz frequency band. (b) Corresponding group velocity dispersion curve obtained by picking the arrival time of the maximum of each correlation envelope at each particular frequency in (a).

region toward the Princes Islands that is located within the shelf region of the northern block (Fig. 6c,d). In this region, the obtained Rayleigh-wave group velocities range from 1.7 to 2.8 km/s for the 0.3–1.0 Hz frequency range. The northwestern section of the Istanbul Peninsula accommodates the lowest velocity values, ranging from 1.7 to 2.4 km/s (green lines). Based on local geologic maps, we find that this area includes the transition between the Thrace basin sediments and the Istanbul zone Paleozoic sediments (Sakınç *et al.*, 1999; Ates *et al.*, 2003), which correlates well with our observation. The rays traveling along the boundary between the Istanbul and Kocaeli Peninsulas show relatively higher values, above 1.9 km/s (light and dark blue lines). There, a slight difference in the obtained dispersion curves is seen despite the similarity in north–south-oriented ray paths. The main difference is that the ray paths represented by light blue lines travel to western Princes Island (Burga-zada), whereas the dark blue ray paths travel toward an eastern Princes Island (Büyükada). The distance between the two islands is 6 km. Most probably, the western side of this particular area is slower than the eastern side.

The third subset represents the region to the south of the Princes Islands, covering the Çınarcık basin and the Armutlu Peninsula (Fig. 6e,f). The green lines are the ray paths sampling the Çınarcık basin. Corresponding dispersion curves again show very low Rayleigh group velocities, ranging from 1.6 to 1.8 km/s for the 0.3–0.6 Hz frequency band, which is similar to the result discussed previously for station pairs sampling the Çınarcık basin (Fig. 6a,b, green lines). Based on the assumption that one-half or one-third of the wavelength corresponds to the penetration depth, this frequency band corresponds to approximate depths of 1.0–4.5 km, which are in the range of the depth of Çınarcık sedimentary basin (Carton *et al.*, 2007). Interestingly, a similar result was reported by Cho *et al.* (2007) for the Korean Peninsula. There, the authors observed lower velocities (by about 4%–10%) to a depth of 5 km in the southeastern part of the peninsula compared with the surrounding tectonic units, indicating the low-velocity material of the Gyeongsang

basin. Furthermore, Nicholson *et al.* (2012) observed similar low velocities down to a depth of 8 km in the Midland Valley and Moray Firth basins by applying ambient noise tomography in the British Isles.

The dispersion curves obtained for the Armutlu Peninsula lie within the 0.3–1.0 Hz frequency band, showing similar group velocities as obtained for the Istanbul and Kocaeli Peninsulas in the north (blue lines in Fig. 6c,d). Based on results obtained from shear-wave splitting analysis, Eken *et al.* (2013) stated the fast polarization direction on the Armutlu Peninsula shows a predominant east–west trend. This is in good correspondence with our results, in which the northwest-trending travel paths extending between Armutlu and Sivriada/Burgazada (Princes Islands) show relatively lower velocity values compared with the observations from east–west-trending travel paths along the Armutlu Peninsula. This indicates that studying ambient noise can also address questions related to crustal anisotropy when sufficient station pairs with travel paths at different azimuths are available.

1D *S*-Wave Velocity Structure Used for Refined Hypocenter Determination

Using the dispersion curves obtained for the eastern Sea of Marmara region, we optimize a 1D *S*-wave velocity model in order to determine improved hypocenter locations for local earthquakes using *S*-phase arrival times detected at stations throughout the region. The dispersion relation of surface waves depends on the penetration depths of different wavelengths and the velocity of the corresponding formation layer through which the waves pass. In principle, shallow layers are sampled by all wavelengths (overdetermined), whereas deeper layers are sampled only by larger wavelengths (underdetermined). The computation of theoretical dispersion curves is based on the eigenvalue problem as described by Haskell (1953) and performed assuming a laterally homogeneous 1D structure consisting of vertically stacked layers with no internal lateral or vertical gradient in compressional wave velocity (V_P), shear-wave velocity (V_S), and density (ρ).
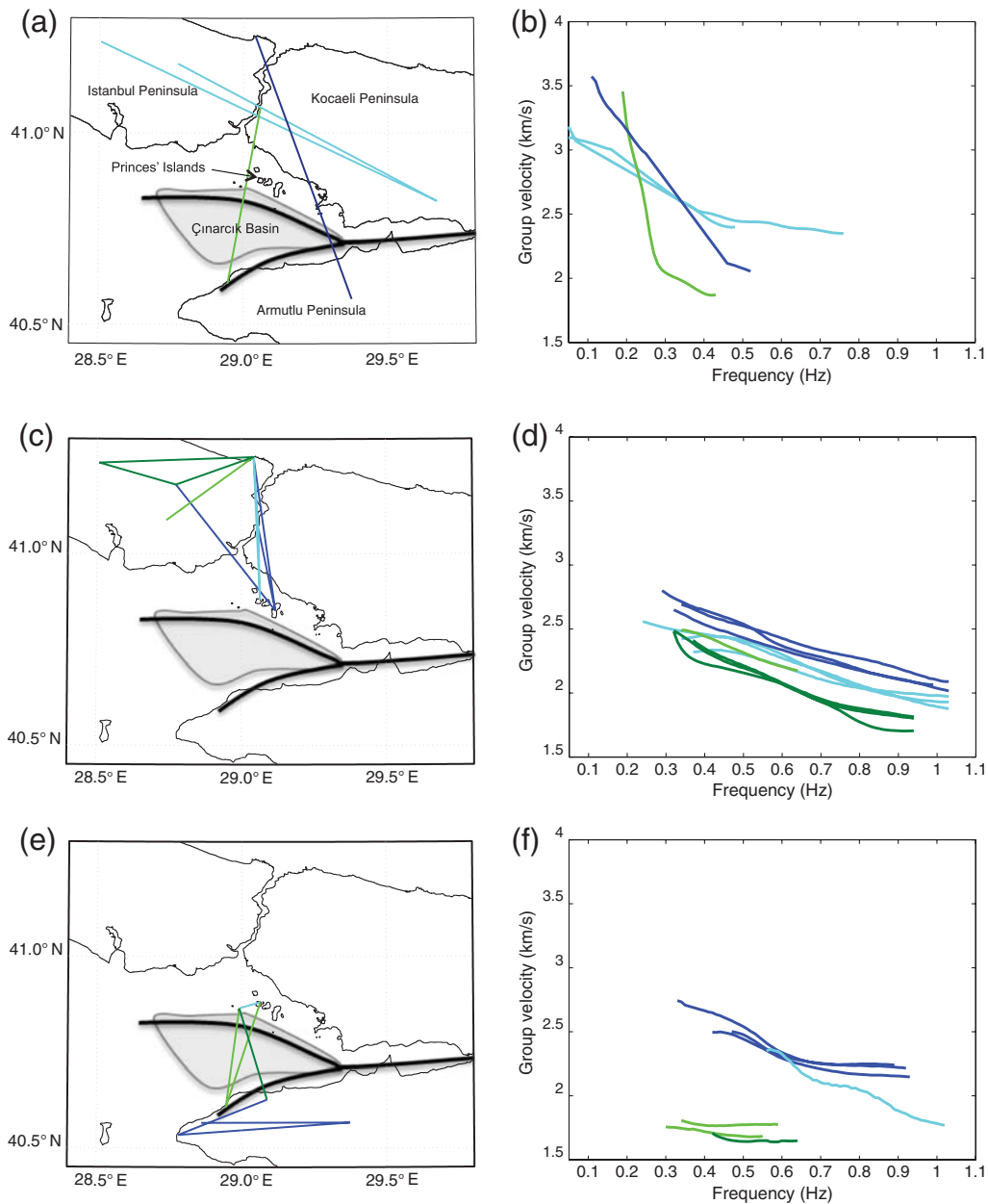
Figure 6. Ray paths (left panels) and group velocity dispersion curves (right panels) for individual station pairs. (a) and (b) are results for ray paths within the northern block and between northern and southern blocks. (c) and (d) are results for ray paths within the northwestern block (Istanbul Peninsula). (e) and (f) are results for the ray paths between islands of the Princes Islands group and within the southern block (Armutlu Peninsula).

Moreover, the thickness is an important parameter to characterize a layer. However, shear-wave velocity is the most influential parameter in the inversion (Xia *et al.*, 2003). In our case, density and *P*-wave velocities are fixed, and only shear-wave velocities are freed during the iterative inversion. The parameter space is searched for the best solution of vertical shear velocities, fixing the depth of interfaces known from an optimized 1D *P*-wave model for the region (Bulut *et al.*, 2009). The inversion problem is linearized using partial derivatives that show how the dispersion velocity at a certain frequency changes with respect to shear-wave velocity perturbation at a

certain depth, and the data misfit is minimized iteratively. The inversion has been performed using the toolbox developed by Herrmann and Ammon (2002) to invert dispersion curves in this frame (SURF96). Following this step, the relocation of the earthquake hypocenters was done using only the *S*-wave arrival times in order to elaborate on the reliability of the *S*-wave velocity model.

We obtain an average dispersion relation (using only good-quality dispersion curves) to be used as input data in order to ensure good stability of the resulting *S*-wave velocity model. The error bounds for the input data are defined using
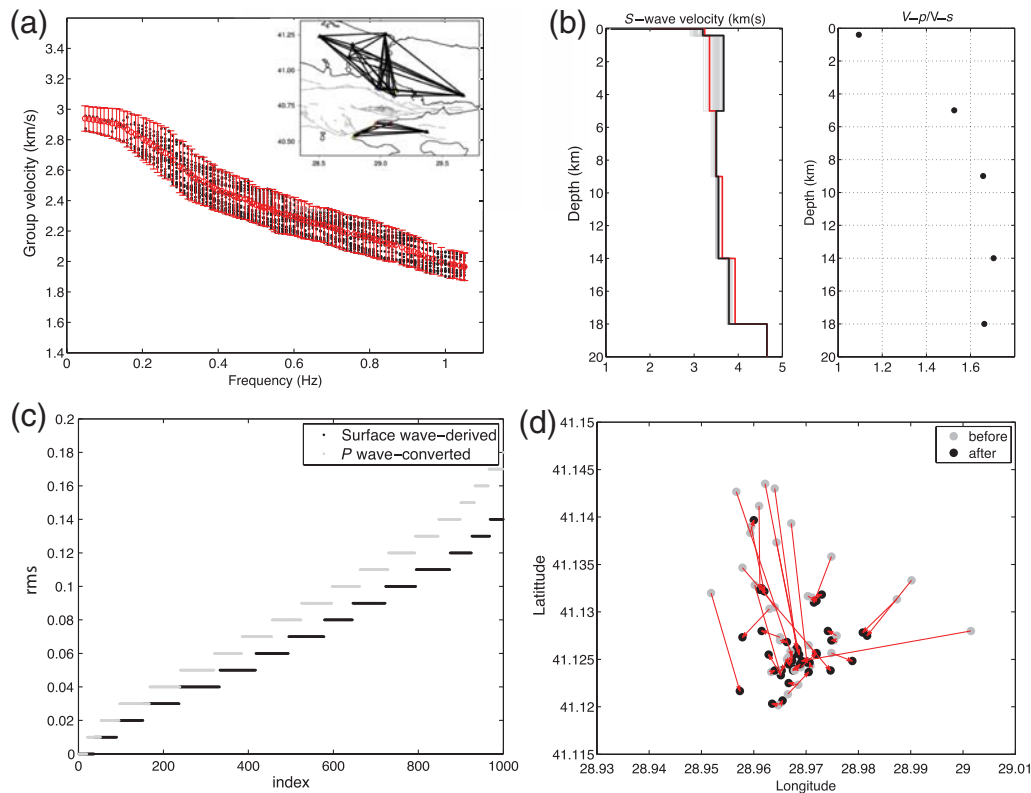
Figure 7. (a) Average dispersion curve and the error bars (red) obtained from the good-quality dispersion curves (black dots) calculated for the target area using continuous ambient noise recordings. Ray paths corresponding to the good-quality dispersion curves are plotted. (b) Left: initial *S*-wave velocity model (red line) as obtained from a regional 1D *P*-wave velocity model using a V_P/V_S ratio of 1.73 (Bulut *et al.*, 2009). The final *S*-wave velocity model after 50 iterations (gray lines) is plotted in black. Within the 0.1–1.1 Hz frequency range, the depth resolution is between approximately 0.6–1 km to 10–15 km. Right: V_P/V_S ratios calculated from the final *S*-wave velocity model derived in this study and *P*-wave velocities from Bulut *et al.* (2009). (c) Data root mean square values obtained after relocation of the earthquake hypocenters using the *P*-wave converted *S*-wave velocity model (black dots) and *S*-wave velocity model obtained in this study (gray dots). A significant improvement can be seen. (d) Hypocentral locations of a selected seismicity below the eastern Sea of Marmara: gray dots are initial locations and black dots are relocated hypocenters using the updated *S*-wave velocity model (*S*-wave velocity [km/s] of [1.11, 3.20, 3.67, 3.50, 3.55, 3.9, 4.65], depths [km] of [0.0, 0.4, 5.9, 9.0, 14.0, 18.0, 30.0]).

the standard deviation of the velocity values for the corresponding frequencies (Fig. 7a). The dispersion curves related to low-velocity structures within the Çınarcık basin were discarded because there is no station right above the basin, and therefore no ray path relevant to hypocenter determination is actually crossing the sedimentary formations (Fig. 2a,b).

The initial *S*-wave velocity model is determined from the existing *P*-wave velocity model (*P*-wave velocities of 3.5, 5.6, 5.8, 6.05, 6.3, 6.8, 8.05 km/s and interfaces at 0, 0.5, 5, 9, 14, 18, 30 km depth; Bulut *et al.*, 2009), using a V_P/V_S ratio of 1.73. The initial iterations are performed using a relatively higher damping factor to avoid overcorrecting the initial model estimates, which might otherwise result in an unreasonable course for model optimization. The iterative process terminated once the error reduction had been stabilized. Interestingly, a low-velocity layer is observed in the resulting *S*-wave velocity model at 5–15 km depth, where most of the seismicity occurs in the region (Bulut and Aktar, 2007; Bulut *et al.*, 2009). The average *S*-wave velocity value of approximately 3.5 km/s at this depth range is in good agreement with

the results obtained from a receiver function study performed based on recordings from 11 broadband stations located in the eastern Sea of Marmara region (Zor *et al.*, 2006). Based on our *S*-wave velocity model, we calculate V_P/V_S ratios for the entire depth range from the surface down to the uppermost mantle (Fig. 7b, right panel). An explanation for the low V_P/V_S ratios at such crustal depths might be that both the 1D *P*- and *S*-wave velocity models simplify a rather heterogeneous velocity field within the uppermost 5 km to a 1D structure. Although there are extensive seismic lines throughout the Sea of Marmara, no active seismic result exists for the onshore areas surrounding the eastern Sea of Marmara (mostly sampled by the ray paths analyzed here). Therefore, a detailed confirmation of the level and depth extent of the velocity inversion proposed here would require onshore seismic profiles throughout the region.

To quantify the improvement provided by our final 1D *S*-wave velocity model (Fig. 7b, left panel) compared with the initial 1D *S*-wave velocity model obtained from the *P*-wave model, we use the root mean square (rms) values for

the (re)calculated earthquake hypocenters. Figure 7c compares the rms values for the final hypocenters that are located using *P*-wave-converted (black dots) and surface-wave-derived *S*-wave velocity models (gray dots). The best quality 1000 events recorded by the local networks in the target area were analyzed for comparison. We show a map view of an earthquake cluster before (gray dots) and after (black dots) the relocation, using the surface-wave-derived *S*-wave velocity structure (Fig. 7d). Relocated earthquake hypocenters represent a narrower cluster compared with the initial diffuse shape. We observe a significant decrease in rms values for the results based on the surface-wave-derived *S*-wave velocity model, confirming the obtained *S*-wave velocity structure allows improvement of hypocenter location quality in the eastern Sea of Marmara region. This observation verifies the reliability of the *S*-wave velocity model obtained using an independent seismological approach.

Conclusions

We successfully applied a cross-correlation analysis of ambient noise surrounding the eastern Sea of Marmara region. Our results are based on observations from 1-year-long continuous waveform data recorded with a combined network consisting of 18 stations from different local, regional, and national networks and interstation distances ranging from 0.3 to 90 km. With this station geometry, we find that at least 60 days of waveform recordings are required to obtain reliable Green's functions. Furthermore, the technique does not work efficiently in case of short-period sensors in our study due to the highly damped frequency content below 1 Hz. The long-distance station pairs above 50 km allow investigation of the dispersion for low-frequency ranges and therefore allow sampling of deeper layers of the crust. The technique is used to investigate the variation of the Rayleigh-wave velocity for the 0.05–1.1 Hz frequency range. We observe the Thrace basin in the northern Istanbul Peninsula hosts a rather lower velocity structure compared with the rest of the crustal block. Moreover, we observe onshore crustal blocks surrounding the eastern Sea of Marmara have similar (higher) seismic velocities, whereas the Çınarcık basin in between reflects lower surface-wave velocities as can be expected. This study has defined the sedimentary and upper crustal *S*-wave velocity structure of the eastern Sea of Marmara region. Furthermore, using an average dispersion curve obtained in this study, we determined a 1D *S*-wave velocity model for the target area, which increases the hypocenter determination precision for seismicity along the Princes Islands segment of the NAFZ offshore of Istanbul from ambient noise recordings.

Data and Resources

The seismic data used in this study are obtained from four different networks. We used data from the PIRES network, which has been operating since autumn 2006. PIRES waveform recordings are open and available through the GeoForschungsZentrums (GFZ) GEOFON webpage (http://geofon.gfz-potsdam.de/waveform/archive/index.php?type=p; last accessed May 2014). Additionally, we included individual regional stations from the nationwide seismic networks operated by the Kandilli Observatory and Earthquake Research Institute (KOERI) in Istanbul and the Turkish Disaster and Emergency Presidency (AFAD) in Ankara. Furthermore, we also included selected stations of the regional permanent network covering the greater Armutlu peninsula area (ARNET). We used Generic Mapping Tools to plot some of the figures (Wessel and Smith, 1995).

Acknowledgments

References

Armijo, R., B. Meyer, S. Navarro, G. King, and A. Barka (2002). Asymmetric slip partitioning in the Sea of Marmara pull-apart: A clue to propagation processes of the North Anatolian fault, *Terra Nova* **14,** no. 2, 80–86.

Asten, M. W. (1978). Geological control of the three-component spectra of Rayleigh-wave microseisms, *Bull. Seismol. Soc. Am.* **68,** no. 6, 1623–1636.

Asten, M. W., and J. D. Henstridge (1984). Arrays estimators and the use of microseisms for reconnaissance of sedimentary basins, *Geophysics* **49,** no. 11, 1828–1837.

Ateş, A., T. Kayıran, and I. Sincer (2003). Structural interpretation of the Marmara region, NW Turkey, from aeromagnetic, seismic and gravity data, *Tectonophysics* **367,** nos. 1/2, 41–99.

Bensen, G. D., M. H. Ritzwoller, M. P. Barmin, A. L. Levshin, F. Lin, M. P. Moschetti, N. M. Shapiro, and Y. Yang (2007). Processing seismic ambient noise data to obtain reliable broad-band surface wave dispersion measurements, *Geophys. J. Int.* **169,** 1239–1260, doi: 10.1111/j.1365-246X.2007.03374.x.

Bensen, G. D., M. H. Ritzwoller, and N. M. Shapiro (2008). Broadband ambient noise surface wave tomography across the United States, *J. Geophys. Res.* **113,** no. B05306, doi: 10.1029/2007JB005248.

Bird, P. (2003). An updated digital model of plate boundaries, *Geochem. Geophys. Geosyst.* **4,** no. 3, 1027, doi: 10.1029/2001GC000252.

Bohnhoff, M., F. Bulut, G. Dresen, P. E. Malin, T. Eken, and M. Aktar (2013). An earthquake gap south of Istanbul, *Nat. Commun.* doi: 10.1038/ncomms2999.

Bonnefoy-Claudet, S., C. Cornou, P.-Y. Bard, and F. Cotton (2004). Nature of noise wavefield, *SESAME Report D13.08,* http://sesame-fp5.obs.ujf-grenoble.fr (last accessed November 2012).

Bulut, F., and M. Aktar (2007). Accurate relocation of İzmit earthquake ($M_w = 7.4$, 1999) aftershocks, *Geophys. Res. Lett.* **34,** L10307, doi: 10.1029/2007GL029611.

Bulut, F., M. Bohnhoff, W. L. Ellsworth, M. Aktar, and G. Dresen (2009). Microseismicity at the North Anatolian fault in the Sea of Marmara offshore Istanbul, *J. Geophys. Res.* doi: 10.1029/2008JB006244.

Bulut, F., W. L. Ellsworth, M. Bohnhoff, M. Aktar, and G. Dresen (2011). Spatiotemporal earthquake clusters along the North Anatolian fault zone offshore Istanbul, *Bull. Seismol. Soc. Am.* **101,** 1759–1768, doi: 10.1785/0120100215.

Carton, H., S. C. Singh, A. Hirn, S. Bazin, B. de Voogd, A. Vigner, A. Ricolleau, S. Cetin, N. Ocakoglu, F. Karakoç, and V. Sevilgen (2007). Seismic imaging of the three-dimensional architecture of the Çınarcık basin along the North Anatolian fault, *J. Geophys. Res.* **112,** no. B06101, doi: 10.1029/2006JB004548.

Chavez-Garcia, F. J., and L. Quintanar (2010). Velocity structure under the Trans-Mexican volcanic belt: Preliminary results using correlation of noise, *Geophys. J. Int.* **183,** 1077–1086.

Cho, K. H., R. B. Herrmann, C. J. Ammon, and K. Lee (2007). Imaging the upper crust of the Korean Peninsula by surface-wave tomography, *Bull. Seismol. Soc. Am.* **97,** no. 1, 198–207.

Eken, T., M. Bohnhoff, F. Bulut, B. Can, and M. Aktar (2013). Crustal anisotropy in the eastern Sea of Marmara region in NW Turkey, *Bull. Seismol. Soc. Am.* **103,** no. 2A, 911–924.

Gallego, A., R. M. Russo, D. Comte, I. Mocanu, R. E. Murdie, and J. C. Vandecar (2010). Seismic noise tomography in the Chile ridge subduction region, *Geophys. J. Int.* **182,** 1478–1492, doi: 10.1111/j.1365-246X.2010.04691.x.

Gülen, L., A. Pınar, D. Kalafat, N. Özel, G. Horasan, M. Yılmazer, and A. M. Işıkara (2002). Surface fault breaks, aftershock distribution and rupture process of the 17 August 1999 Izmit, Turkey, earthquake, *Bull. Seismol. Soc. Am.* **92,** no. 1, 230–244.

Haskell, N. A. (1953). The dispersion of surface waves on multilayered media, *Bull. Seismol. Soc. Am.* **43,** 17–34.

Herrmann, R. B., and C. J. Ammon (2002). *Computer Programs in Seismology*, Vol. IV, St. Louis University, Missouri.

Karabulut, H., S. Özalaybey, T. Taymaz, M. Aktar, O. Selvi, and A. Kocaoğlu (2003). A tomographic image of the shallow crustal structure in the eastern Marmara, *Geophys. Res. Lett.* **30,** no. 24, 2277.

Lin, F. C., M. P. Moschetti, and M. H. Ritzwoller (2008). Surface wave tomography of the western United States from ambient seismic noise: Rayleigh and Love wave phase velocity maps, *Geophys. J. Int.* **173,** 281–298.

Nicolson, H., A. Curtis, B. Baptie, and E. Galetti (2012). Seismic interferometry and ambient noise tomography in the British Isles, *Proc. Geol. Ass.* **123,** 74–86.

Parsons, T. (2004). Recalculated probability of *M* 7 earthquakes beneath the Sea of Marmara, Turkey, *J. Geophys. Res.* **109,** no. B05304, doi: 10.1029/2003JB002667.

Renalier, F., D. Jongmans, M. Campillo, and P.-Y. Bard (2010). Shear wave velocity of the Avignonet landslide (France) using ambient noise correlation, *J. Geophys. Res. Earth Surface* **115,** no. F3, doi: 10.1029/2009JF001538.

Sakınç, M., C. Yaltırak, and F. Y. Oktay (1999). Palaeogeographical evolution of the Thrace Neogene basin and the Tethys–Parathetys relations at northwestern Turkey (Thrace), *Palaeogeogr. Palaeoclimatol. Palaeoecol.*, **153,** 17–40.

Shapiro, N. M., and M. Campillo (2004). Emergence of broadband Rayleigh waves from correlations of ambient seismic noise, *Geophys. Res. Lett.* **31,** L07614, doi: 10.1029/2004GL019491.

Shapiro, N. M., M. Campillo, L. Stehly, and M. H. Ritzwoller (2005). High resolution surface-wave tomography from ambient seismic noise, *Science* **307,** no. 5715, 1615–1618.

Tunç, B., D. Caka, T. S. Irmak, H. Woith, S. Tunç, S. Barış, M. F. Özer, B. G. Lühr, E. Günther, H. Grosser, and J. Zschau (2011). The Armutlu Network: An investigation into the seismotectonic setting of Armutlu-Yalova-Gemlik and the surrounding regions, *Ann. Geophys.* **54,** no. 1, doi: 10.4401/ag-4877.

Wessel, P., and W. H. F. Smith (1995). New version of the generic mapping tools released, *Eos Trans. AGU* **76,** no. 33, 329, doi: 10.1029/95EO00198.

Xia, J., R. D. Miller, C. B. Park, and G. Tian (2003). Inversion of high frequency surface waves with fundamental and higher modes, *J. Appl. Geophys.* **52,** 45–57.

Zor, E., S. Özalaybey, and C. Gürbüz (2006). The crustal structure of the eastern Marmara region, Turkey by teleseismic receiver functions, *Geophys. J. Int.* **167,** 213–222.

GFZ German Research Center for Geosciences
Section 3.2 Geomechanics and Rheology
Telegrafenberg, 14473 Potsdam, Germany
acarel@gfz-potsdam.de
bulut@gfz-potsdam.de
bohnhoff@gfz-potsdam.de